Characterisation of the current switch mechanism in two-stage wire array Z-pinches

G. C. Burdiak, S. V. Lebedev, A. J. Harvey-Thompson, G. N. Hall, G. F. Swadling, F. Suzuki-Vidal, E. Khoory, S. N. Bland, L. Pickworth, P. de Grouchy, J. Skidmore, L. Suttle, and E. M. Waisman

---

Articles you may be interested in
Radiative cooling of two-component wire-array Z-pinch plasma
Phys. Plasmas **21**, 082704 (2014); 10.1063/1.4892180

Opacity and gradients in aluminum wire array z-pinch implosions on the Z pulsed power facility
Phys. Plasmas **21**, 031201 (2014); 10.1063/1.4865224

Ablation dynamics in coiled wire-array Z-pinches
Phys. Plasmas **20**, 022703 (2013); 10.1063/1.4789851

Neutron emission generated during wire array Z-pinch implosion onto deuterated fiber
Phys. Plasmas **15**, 032701 (2008); 10.1063/1.2839352

The dynamics of wire array Z-pinch implosions
Phys. Plasmas **6**, 2016 (1999); 10.1063/1.873456

Characterisation of the current switch mechanism in two-stage wire array Z-pinches

G. C. Burdiak,[1] S. V. Lebedev,[1] A. J. Harvey-Thompson,[1,a)] G. N. Hall,[1,b)] G. F. Swadling,[1]
F. Suzuki-Vidal,[1] E. Khoory,[1,c)] S. N. Bland,[1] L. Pickworth,[1,b)] P. de Grouchy,[1,d)]
J. Skidmore,[1,e)] L. Suttle,[1] and E. M. Waisman[2]

[1]*Blackett Laboratory, Imperial College, London SW7 2BW, United Kingdom*
[2]*Sandia National Laboratories, Albuquerque, New Mexico 87185-1106, USA*

In this paper, we describe the operation of a two-stage wire array z-pinch driven by the 1.4 MA, 240 ns rise-time Magpie pulsed-power device at Imperial College London. In this setup, an inverse wire array acts as a fast current switch, delivering a current pre-pulse into a cylindrical load wire array, before rapidly switching the majority of the generator current into the load after a 100–150 ns dwell time. A detailed analysis of the evolution of the load array during the pre-pulse is presented. Measurements of the load resistivity and energy deposition suggest significant bulk heating of the array mass occurs. The ∼5 kA pre-pulse delivers ∼0.8 J of energy to the load, leaving it in a mixed, predominantly liquid-vapour state. The main current switch occurs as the inverse array begins to explode and plasma expands into the load region. Electrical and imaging diagnostics indicate that the main current switch may evolve in part as a plasma flow switch, driven by the expansion of a magnetic cavity and plasma bubble along the length of the load array. Analysis of implosion trajectories suggests that approximately 1 MA switches into the load in 100 ns, corresponding to a doubling of the generator dI/dt. Potential scaling of the device to higher current machines is discussed. © 2015 AIP Publishing LLC. [http://dx.doi.org/10.1063/1.4936278]

I. INTRODUCTION

Cylindrical wire array z-pinch implosions are excellent sources of soft x-rays[1] and k-shell radiation.[2] Their behaviour is well characterised and reproducible, and experiments involving multiple nested wire arrays have demonstrated radiation pulse-shaping.[3] Most applications, for example, inertial confinement fusion (ICF), radiation science, and laboratory astrophysics, require a high power x-ray source. Experiments and analytical models[4] have shown that to produce a high power source, the rise-time for the current pulse that drives the z-pinch load should be minimised. Accordingly, for a given load inductance, this requires an increasingly high voltage generator, which is both expensive and difficult to engineer.

A potential way forward for existing pulsed-power devices is to dynamically sharpen the current pulse by introducing a plasma current switch as an integral part of the z-pinch load. Fast plasma switches have been extensively studied as the final stage in generator power feeds, and there are several mechanisms for their operation. Plasma flow switches (PFSs) operate by magnetic acceleration of a plasma discharge along a coaxial vacuum power feed. The PFS may deliver current to the load by bridging a deliberate gap between the load and the generator.[5,6] Alternatively, the PFS may switch current by opening in parallel to the load as the discharge expands within the vacuum.[7] A review of plasma flow switches can be found in Ref. 8. Plasma erosion opening switches (PEOSs) involve the erosion of an auxiliary conducting plasma channel positioned in parallel to the load.[9,10] These devices were first investigated as a means to reduce current pre-pulse into diode experiments.[11,12] PEOSs will often exhibit some flow switch behaviour, as the eroding plasma channel will be, to some extent, swept along the power feed by the $\mathbf{J} \times \mathbf{B}$ force.[13–15] Plasma switches have been successful at sharpening generator current profiles, although the operation tends to become lossy at high voltages and currents.

Another important aspect of wire array operation is the existence of an extended ablation phase[16–21] before the main implosion. During this phase, which may last 50%–80% of the total implosion time, plasma is continuously generated at the surface of the dense, stationary wire cores and accelerated towards the axis by the $\mathbf{J} \times \mathbf{B}$ force. This causes significant radial redistribution of the array mass before the start of the main implosion. Importantly, ablation proceeds in a non-uniform way along each wire, with an axial modulation of the ablation rate. This creates highly non-uniform initial conditions for the main (snowplough-like) implosion phase,[22] causing some fraction of the array mass to be left behind at large radius. This trailing mass limits the convergence of the current toward the axis, and hence limits x-ray power produced at stagnation of the pinch.

a)Present address: Sandia National Laboratories, Albuquerque, New Mexico 87185-1106, USA.
b)Present address: Lawrence Livermore National Laboratory, Livermore, California 94550, USA.
c)Present address: Science Research Laboratory, Dubai Government, P.O. Box 548, Al Qusais, Dubai, UAE.
d)Present address: Laboratory of Plasma Studies, Cornell University, Ithaca, New York 14853, USA.
e)Present address: Atomic Weapons Establishment, Aldermaston RG7 4PR, United Kingdom.

    22, 112710-1

Two-stage wire array z-pinch loads have been proposed as a means to both sharpen the current profile and suppress or control the ablation phase.[23] A two-stage wire array z-pinch consists of a parallel arrangement of two cylindrical arrays, as shown in Fig. 1. The bottom array is arranged in an inverse (exploding) configuration, and the top (load) array is arranged in a standard imploding geometry. The inverse array consists of wires positioned around a central cathode rod such that the $\mathbf{J} \times \mathbf{B}$ force acts radially outward on the wire material, as opposed to radially inward for the load array geometry.

In this setup, the inverse array acts both as a generator for a current pre-pulse into the load array, and also as a fast current switch that provides a ~100 ns delay between the pre-pulse and the main current pulse into the load. Previous work has shown[23] that preconditioning of the load array in this manner dramatically alters the ensuing load implosion dynamics; the ablation phase is eliminated, and no trailing mass remains at the initial array radius during the final implosion. The inverse array provides intermediate inductive energy storage to drive the load implosion. The dynamics of the implosion suggest that a significant fraction of the total generator current is switched into the load, with a rise-time of approximately half that of the Magpie generator driving the experiment. However, all attempts to measure the load current profile using our standard diagnostics have failed to provide results consistent with load current profiles inferred from implosion dynamics.

In this paper, we present detailed data and analysis on the operation of two-stage wire arrays, with a particular emphasis on the interpretation of electrical measurements. First, in Sec. II, we detail the experimental setup and give an overview of two-stage wire array evolution. In Sec. III, we characterise the evolution of the load array during the current pre-pulse using measurements of resistivity and resistive energy deposition. The remainder of the paper is dedicated to the operation of the main current switch. Sec. IV A describes our initial attempts to measure the load current during the current switch and the associated issues. In Sec. IV B, we detail a new static load magnetic field diagnostic designed specifically to measure the load current profile. In Sec. IV C, we discuss results obtained with this diagnostic and describe our present understanding of the current switch mechanism. In Sec. IV D, we provide estimates for the load current and make comparisons to implosion data using a 0D implosion model. In Sec. V, we discuss possibilities for scaling of the two-stage wire array configuration to higher current machines. Conclusions are presented in Sec. VI.

II. EXPERIMENTAL SETUP AND OVERVIEW OF TWO-STAGE WIRE ARRAY OPERATION

A. Experimental setup

A schematic diagram of the experimental setup and electrical diagnostics is shown in Fig. 1(b). For clarity throughout this paper, the top array in the diagram is consistently referred to as the load or imploding array, the bottom array as the inverse or exploding array, and the complete, two stage configuration as the total load or two-stage array. Experiments were performed on the 1.4 MA, 240 ns rise-time Magpie facility at Imperial College London.[24] Inverse arrays were 16 mm in diameter and consisted of 8×12.5–15 μm evenly spaced aluminium (Al) wires, surrounding an 8 mm diameter cylindrical cathode rod. Inverse array lengths varied from 34–50 mm. Load arrays were 8–17 mm in diameter and consisted of 8×10–15 μm Al wires, with lengths varying from 16–42 mm. In several experiments, the load array was replaced by a static (non-imploding) load with embedded B-dot (dB/dt) monitors. The current return structure is arranged on two levels (above and below the "anode" in Fig. 1(b)) so that the load array and total load current can be monitored separately. These return structures are each composed of 8 mm diameter posts evenly spaced at a distance of 77.5 mm from the array axis. There are 4 posts on the upper level to allow for unrestricted diagnostic access to the experiment, and 16 posts on the lower level to minimise inductance. For construction purposes, there is a 5–8 mm connecting section between the two arrays. Plasma dynamics were diagnosed using a suite of imaging diagnostics, including an optical streak camera, 12-frame optical framing camera (5 ns exposure), 4-frame extreme ultraviolet (XUV) pinhole cameras (5 ns exposure), and several laser probing channels (300 mJ, 0.5 ns, 532 nm) for interferometry and shadowgraphy imaging. Electrical load properties were monitored using several Rogowski groove dI/dt monitors (positioned as shown in Fig. 1), a resistive voltage probe connected in parallel to the inverse and load arrays, and B-dot probes embedded in the low voltage side of the magnetically insulated transmission line (MITL) of the generator. A continuous-wave (CW) Faraday rotation diagnostic was also fielded during several experiments. All of the electrical diagnostics are discussed more thoroughly at relevant points throughout the paper.
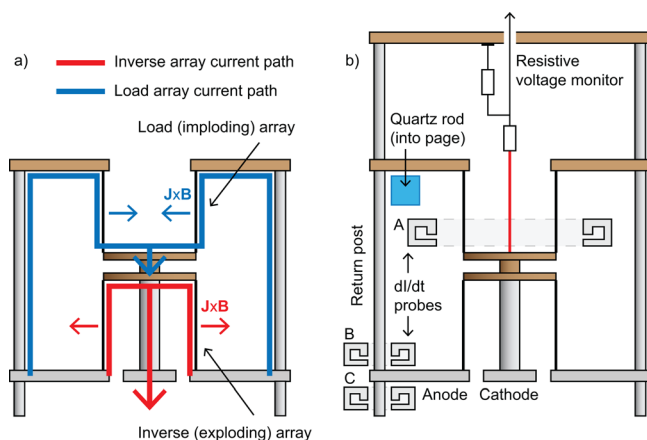

FIG. 1. Schematic diagrams of a two-stage wire array z-pinch. The inverse (exploding) and load (imploding) cylindrical wire arrays are connected in electrical parallel to the generator voltage. (a) Idealised current paths through the inverse and load arrays. (b) Electrical diagnostics: Rogowski groove dI/dt monitors mounted around return posts and the load; quartz rod used for CW Faraday rotation measurements; voltage monitor mounted end-on to the load for measurements of the resistive component of the load voltage. The probe connection (red) draws no current from the generator.

B. Overview of the operation of a two-stage wire array z-pinch

Inverse arrays have been shown to exhibit the same ablation dynamics as standard wire array z-pinches, with the exception that the ablation flow is directed radially outwards.[25,26] At the beginning of the generator current pulse, energy is deposited into the array wires via resistive heating. This "resistive phase" lasts for $\sim$20 ns and ends when plasma forms on the surface of the wires. At this point, surface plasma begins to ablate radially outwards, with the ablation flow being continuously fed by new material from the stationary wire cores. As in the case of standard cylindrical arrays, there is a periodic axial modulation to the ablation rate. The ablation phase ends when approximately 50% of the initial array mass has been ablated, and gaps begin to appear in the wire cores. This signals the beginning of the main explosion of the array. Significant trailing mass is left at the initial wire radius, and magneto-Rayleigh-Taylor (MRT) instabilities develop in the magnetically driven flow. Aside from the short resistive phase, the voltage across the inverse array wires (measured at the top of the central cathode rod) remains very low until the explosion of the array.[25] When the explosion begins, the impedance (resistance and inductance) of the wires, and therefore the voltage across them, rapidly increases. This characteristic voltage history makes the inverse array a promising, compact tool for rapidly switching current into a load.

In the two-stage array configuration, the inverse array behaves in the same way as an isolated inverse array. The early-time resistive phase is responsible for a current pre-pulse into the load array. During this time, current is resistively divided between the two arrays, taking both the red and blue paths indicated in Fig. 1(a). The energy deposited into the load during the pre-pulse is sufficient to begin to bulk vapourise the load wires. The pre-pulse ends when plasma forms on the surface of the inverse array wires. At this point, an inductive current division takes over (resistance becomes negligible), and the majority of the generator current flows through the relatively low inductance inverse array (red path in Fig. 1(a)). The load array experiences a 100–150 ns current free "dwell phase" coincident with the ablation phase of the inverse array. During this time, the load array wires thermally expand into the vacuum to a diameter of $\sim$1 mm. The dwell phase ends as gaps form in the wires of the inverse array and it begins to explode. At this point, current begins to switch from the inverse array into the load, taking the blue path in Fig. 1(a). Upon switching, all of the load array mass is rapidly ionised. The preconditioned load wires do not exhibit the core-corona structure that is ubiquitous in all standard wire array experiments. As a result, the usual wire array ablation phase is suppressed, and a 0D-like implosion of the load array ensues, leaving negligible trailing mass at the initial wire radius.

The optical emission time series in Fig. 2 shows the evolution of a two-stage wire array z-pinch from the dwell phase through to stagnation of the load array. In the first 3 frames, plasma can be seen ablating radially outwards from the inverse array. There is no emission from the load at this time because very little current flows through it. In the third frame, axial
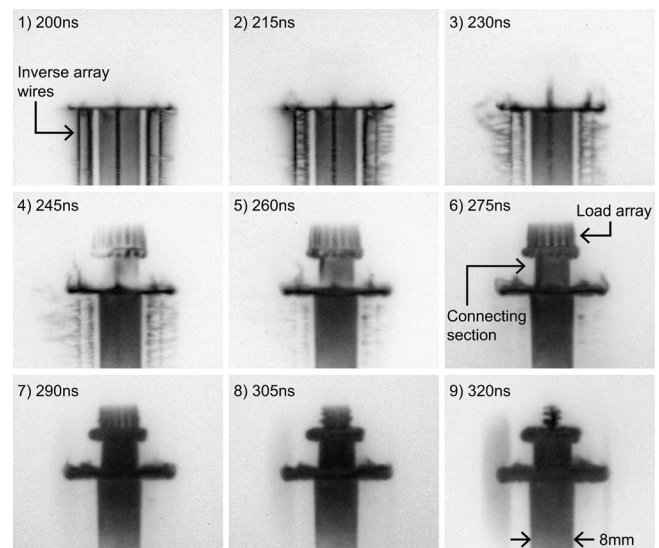

FIG. 2. Optical emission time-series showing the evolution of a two-stage wire array z-pinch. The field of view includes the top 14 mm of the 50 mm inverse array and the bottom 4 mm of the 16 mm long, 8 mm Ø load array. There is a 7 mm connecting section between the two arrays.

breaks in the inverse wire cores first appear, and current begins to switch into the load. In the fourth frame, the inverse array begins to explode and emission from the expanded ($\sim$1 mm) load array wires can clearly be seen. In the ensuing frames, the load array is seen to implode, and the remaining inverse array plasma becomes too tenuous to be detected by the camera.

III. PRECONDITIONING OF THE LOAD ARRAY AND ENERGY DEPOSITION DURING THE CURRENT PRE-PULSE

Preconditioning of the load array and the resultant modifications to the load implosion dynamics were first described in Ref. 23. Here, we present a much more detailed account and analysis of electrical measurements obtained during the current pre-pulse.

A series of experiments were performed to characterise the evolution of the load array during the pre-pulse phase. Simultaneous, independent measurements of the load current and the resistive component of the load voltage were obtained in order to determine (a) the energy deposited within the load array and (b) the resistance history of the load array. These independent measurements allow energy deposition and resistance to be determined without the need to make assumptions about the resistivity, heat capacity, and uniformity of the load. The resistive probe used to monitor the load voltage was described in detail in Ref. 27. For these measurements, the voltage probe is suspended vertically above the experimental load hardware, and the electrical connection from the probe to the high voltage electrode of the load is made along the axis of the load array, as shown schematically in Fig. 1(b). This technique, as described in Ref. 28, ensures that the probe is sensitive only to the resistive component of the load voltage, V_R; negligible magnetic flux associated with time-varying current through the load threads the current loop of the voltage probe connection. The current through the load was monitored using Rogowski

groove dI/dt monitors fielded on current return posts. Signals were recorded on a 10 GHz oscilloscope, to collect many data points over the short ($\sim$20 ns) pre-pulse. Four experiments were performed with inverse and load arrays 16 mm in diameter, each consisting of $8 \times 12.5\,\mu m$ diameter Al (5056 alloy) wires. The exploder length was fixed at 34 mm for all experiments whilst the load array length was varied between 20 and 30 mm. Repeating the experiment with different load array lengths allowed us to assess the importance of electrode contact resistance.

Figure 3 shows V_R, dI/dt and current traces from an experiment with a 24 mm long load array. A 5 kA current pulse is driven into the load via predominantly resistive current division between the inverse and load arrays. A peak voltage of 35 kV develops across the load as a result of resistive heating. The voltage decays to zero as plasma forms on the inverse array wires and remains at zero for the next $\sim$100 ns until the beginning of the main current switch. This indicates that the voltage probe is indeed only sensitive to the resistive component of the load voltage, despite the inductive component reaching over $\sim$100 kV during this time. The width of the voltage pulse ($\sim$15 ns) defines the timespan for energy deposition within the load array, despite the fact that a small amount of current continues to flow in the load, driven by inductive current division heavily biased toward the low inductance inverse array.[23,25]

Energy deposition was determined from the experimental data by numerical computation of the following integral:

$$\Delta Q(t) = \int_0^t V_R(t)I(t)dt. \tag{1}$$

The energy delivered to 4 different loads as a function of time is shown in Fig. 4(a). With the exception of the 27 mm array, energy deposition begins coincidently and the total energy delivered is approximately the same (0.7–0.9 J) in each case. The experiment with the 27 mm load suffered from a significant generator pre-pulse caused by non-simultaneous firing of the four pulse-forming lines.[24] Because the experiments were
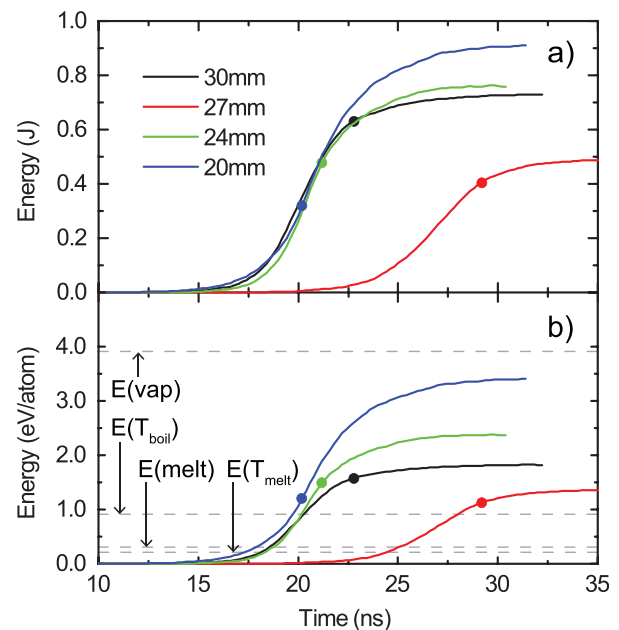
FIG. 4. Energy deposition into load arrays with different lengths (all 16 mm Ø, $8 \times 12.5\,\mu m$ Al) during the current pre-pulse. Inverse array dimensions were fixed between experiments. The upper panel (a) is in units of J. The lower panel (b) is in normalised units of eV/atom. Spots represent the time at which *bulk* heating probably ceases during each experiment, based on results in Fig. 5. Dashed horizontal lines represent E required to reach T_{melt}, E required for bulk melting, E required to reach T_{boil} and E required for bulk vapourisation.

carried out with loads of different lengths, it is instructive to replot the data in normalised units of eV/atom, as in Fig. 4(b). In this plot, it is assumed that energy deposition occurs uniformly throughout the bulk and along the length of the wires. Significantly more energy is deposited per atom as the load array length is reduced. In all cases, sufficient energy ($>$0.9 eV) is deposited to melt the load and raise the temperature to the vapour point. A total of 3.9 eV/atom is required to fully atomise the load material; this is greater than the energy delivered by the pre-pulse in all cases. Therefore, by the end of the pre-pulse, the load likely exists as a liquid-vapour mixture. This observation is consistent with previously published[23] interferometric results that show the line integrated atom density ($n_a l$) after a period of thermal expansion is slightly lower than would be expected given the number of atoms in the wire, suggesting the presence of liquid droplets that are not detected by the interferometer. Additional measurements concerning the detailed radial structure of preconditioned, expanded wire cores will be published separately.

The evolution of the load material resistivity during the pre-pulse was calculated using the following formula:

$$\rho(t) = \frac{V_R(t)NA}{I(t)l}, \tag{2}$$

where V_R and I are measured quantities, N is the number of wires, A is the cross-sectional area of each wire, and l is the wire length. The area A was taken as the initial value for the cold wire, since the pre-pulse occurs on a timescale much shorter than the timescale for thermal expansion. For constant area and length, the resistivity depends only on the
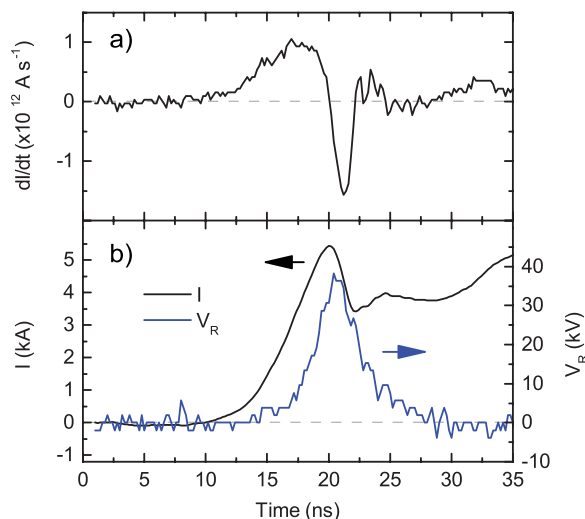
FIG. 3. Electrical signals characterising the current pre-pulse into a 24 mm load array. (a) Load array dI/dt. (b) Load current deduced from dI/dt signal (black) and resistive load voltage (blue).

temperature ($\rho = \rho(T)$). Furthermore, for a fixed mass, the temperature depends only on the energy deposited ($Q = Q(T)$). Consequently, we can say that the resistivity is a function of energy deposition only ($\rho = \rho(Q)$) and should be independent of the time history of the resistive heating, the pre-pulse current and voltage temporal profiles, and the array geometry. By combining results from Eqs. (1) and (2), it is possible to determine $\rho(Q)$ using the experimental data. Plots of $\rho(Q)$ for each experiment are given in Fig. 5. Given that $\rho = \rho(Q)$ only, the plots in Fig. 5 provide a consistency check between experiments. It can be seen that agreement between datasets is generally good during the earlier stages of energy deposition.

The dashed dark green line in Fig. 5 represents the expected $\rho(Q)$ from a simple theoretical model. Within this model, the energy deposition required to bring about a given temperature change of the wire material, taking into account phase transitions, was determined via the following formula:

$$\Delta Q(T) = \int_{298K}^{T} c(T)\, dT + \Delta H^{melt}|_{T \geq 934K} + \Delta H^{vap}|_{T \geq 2790K}.$$

(3)

$c(T)$ is the Al heat capacity and was found from standard heat capacity data tables. The linear temperature dependence of the solid phase Al heat capacity was approximated as a single average value of 3.0×10^{-4} eV/K/atom. Al heat capacity in the liquid phase has an almost constant value of 3.3×10^{-4} eV/K/atom. ΔH^{melt} and ΔH^{vap} are the enthalpies of fusion (0.11 eV/atom) and vapourisation (2.95 eV/atom) and are only relevant at or above T_{melt} (934 K) and T_{boil} (2790 K), respectively. $\Delta Q(T)$ was calculated numerically via Eq. (3) and used together with standard resistivity ($\rho(T)$) data tables in order to plot the $\rho(Q)$ model.

During the early stages of energy deposition, the load resistivity increases as the temperature rises. The data from each experiment show good agreement with the model during this stage, strongly suggesting significant bulk heating and negligible electrode contact resistance. The gradient of

the liquid-heating line in the model is particularly well matched by data from the 27 mm and 30 mm load arrays. The turning points in the experimental data probably correspond to some degree of plasma formation on the load array wires, occurring before bulk vapourisation of the load. Comparisons of temporally resolved energy deposition to expected bulk thermodynamic characteristics are only reliable up to the times corresponding to these turning points. These times have been indicated in Fig. 4. Imaging data obtained at $\sim$100 ns after the pre-pulse show significantly less thermal expansion of the 2–3 mm load region closest to the anode, regardless of the length of the array. We speculate that the electric field close to the anode could be responsible for the reduced energy deposition in the wire cores in this region and the possible formation of an axially localised plasma layer surrounding the wire cores. The increased significance of this effect for shorter loads could explain the deviation of the experimental data from the model for the 20 mm array. The anode end-effect has since been successfully mitigated via careful shaping of the electrode. This was found to significantly increase the uniformity of the implosion of the load array after the main current switch; data from these experiments will be presented in a separate publication.

IV. CHARACTERISATION OF THE CURRENT SWITCH MECHANISM

A. Initial attempts to measure current in the load array

Rogowski groove dI/dt monitors are routinely and reliably fielded on current return posts during all Magpie experiments in order to determine the load current via numerical (not passive) integration of the signal. However, attempts to measure the load current using Rogowski grooves during the switching phase of 2-stage wire array experiments have not been fully successful. Reasons for this will be discussed thoroughly in Sec. IV C.

Rogowski probes positioned around the load array (position A) or around current return posts (position B), as shown in Fig. 1(b), invariably produce signals that contradict the load array implosion dynamics or else fail to operate throughout timescales of interest. An example signal from a Rogowski probe mounted around a current return post is shown in Fig. 6(a), along with the form of the total generator dI/dt signal as measured by a B-dot probe embedded in the low voltage side of the vacuum transmission line (MITL). The Rogowski signal appears to show the beginning of the current switch into the load. However, very rapidly the signal saturates, which may indicate a breakdown of the probe (this is not oscilloscope saturation). The rapid rise in the load current upon switching can generate sufficient voltage ($\sim$kV) on the probes to cause electrical breakdown either across the probe gap or within the coaxial cable connected to it. Additionally, the probe gap can be short circuited by the flow of plasma from the inverse (exploding) array. Probes surrounding the load array are also susceptible to electrical noise and capacitive coupling to the generator or other parts of the load. The start of the switching of current into the load results in a dip in the generator dI/dt as measured by the MITL B-dot. There is a clear delay of 20 ns between the
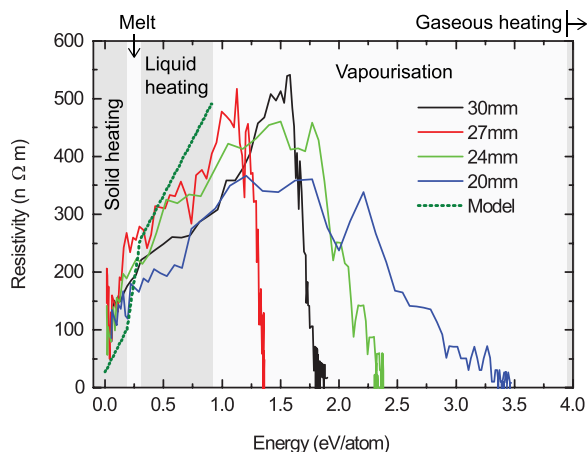
FIG. 5. Average load resistivity as a function of energy deposited during the current pre-pulse. Experimental data plotted as solid lines. Theoretical resistivity model plotted as a dashed line. Grey shading represents different thermodynamic states for a given internal energy (independent of resistivity model).
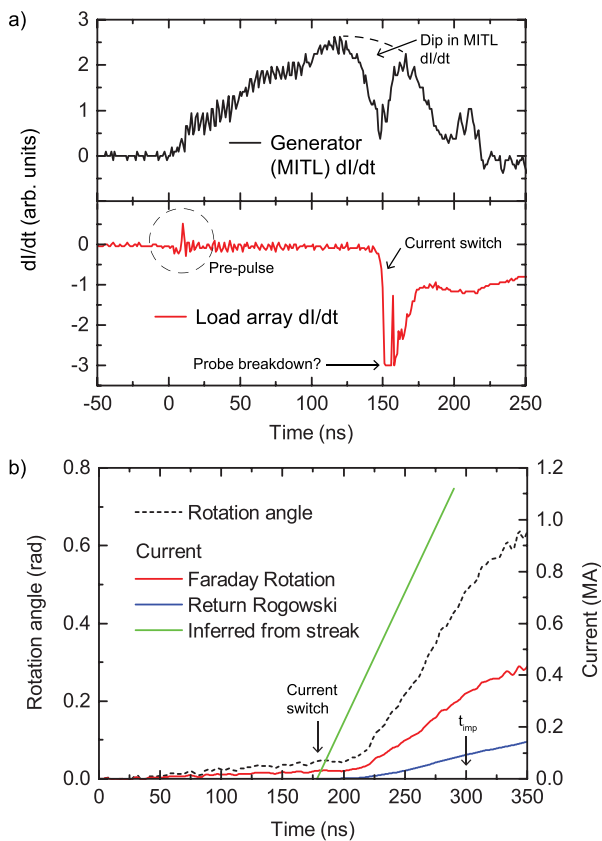
FIG. 6. a) Waveforms for dI/dt of the generator and dI/dt through the load array. The onset of the main current switch into the load array causes a dip in the dI/dt of the generator. Data first presented in Ref. 23. (b) Load current profiles as measured by a CW Faraday rotation diagnostic (red line) and return post Rogowski probe (blue line).[29] The dashed line shows the rotation angle of the Faraday probe. The drive current inferred from the implosion trajectory of the load array is given by the green line. t_{imp} gives the time for peak x-ray power at stagnation. Data in (a) and (b) are from separate experiments.

generator response and the Rogowski probe signal, suggesting that the Rogowski is not sensitive to the initial stages of the current switch. The saturation and delay of Rogowski signals means that we cannot use them to reliably determine the load current. If integration of the Rogowski dI/dt signals is carried out regardless, we find that in all cases, whether probe saturation/breakdown occurred or not, the resulting current is never large enough to account for the rapid implosion of the load array as observed in optical streak images and other diagnostics. The failure to determine the current by measuring dB/dt at a large radial distance from the load, via pickup of azimuthal field surrounding either the current return posts or the wire array load itself, may indicate alternative current paths to those suggested in Fig. 1(a).

The argument for alternative current paths is further strengthened by attempts to measure the current in the load using a CW Faraday rotation diagnostic. A detailed description of this diagnostic can be found in Ref. 29. The diagnostic utilises a 100 mm long quartz rod (Verdet constant = 5 rad T^{-1} m^{-1} at 532 nm) as the Faraday medium and a 70 mW, 532 nm, plane polarised CW laser probe. The rod is positioned between the load and current return structure, so that it is bathed in azimuthal magnetic field from the axial current pulse. The polarisation plane of the probe laser is rotated by

magnetic field oriented parallel to the laser propagation vector, with the rotation angle proportional to the line integrated strength of the magnetic field along the rod. Orthogonal polarisation vectors were split after the rod using a polarising beam splitter, and the intensity of each component was monitored with photodiodes in order to determine the rotation angle. The diagnostic successfully measured the full load current history during standard cylindrical wire array experiments, showing excellent agreement between Faraday and Rogowski current measurements.[29] During two-stage array experiments, the rod was positioned high up in the current return structure as indicated in Fig. 1(b), with the centre of the rod at a distance of 65 mm from the array axis (cf. return posts are centered 77.5 mm from the array axis). Fig. 6(b) shows load current profiles deduced from Faraday rotation and Rogowski measurements, together with the drive current inferred from the implosion trajectory from the same experiment. Details concerning the inference of the drive current from implosion trajectories are presented in Sec. IV D. Note that the data in Figs. 6(a) and 6(b) are from separate experiments. The Faraday diagnostic measured a load current of just 350 kA at the time of peak x-ray power (300 ns) and the current rise rate appears to be even less than that during a standard cylindrical wire array Magpie experiment. By comparison to the current profile inferred from the implosion trajectory, it is clear that the Faraday current profile is not steep enough to account for the rapid (120 ns) implosion of the array mass. The return post Rogowski probes on this experiment measured even less current than the Faraday diagnostic. Despite the issues with these diagnostics, it is significant that similar effects have been observed using both electrical (dB/dt) and optical techniques. We can be confident that the Rogowski probes measure the true dB/dt at their position, and that the signals they pick up are not dominated by electrostatic noise.

These results strongly suggest that at all times after the main current switch, there exists a radially distributed current return path that is not localised to the current return posts. This means that the load current cannot be accurately determined by making measurements of the magnetic field at large radius. The necessary standoff of Rogowski probes and CW Faraday diagnostics from the load array means that they could never measure the full load current. In addition, the different positions of the Faraday and Rogowski magnetic field measurements may impact upon their relative sensitivity to the load current. To overcome these difficulties and gain a greater understanding of the current switch process, experiments have been performed with the specific aim of measuring the current directly in the load. The design and calibration of the load used to make these measurements is presented in Section IV B.

B. Design of a B-dot diagnostic for monitoring dI/dt within a static load

A schematic of the experimental setup designed to understand the current switch mechanism of 2-stage wire array z-pinches is shown in Fig. 7. In these experiments, the load array was replaced by a static brass cylinder with two inserted B-dot probes positioned close to the bottom of two cavities. Time-varying magnetic flux associated with current
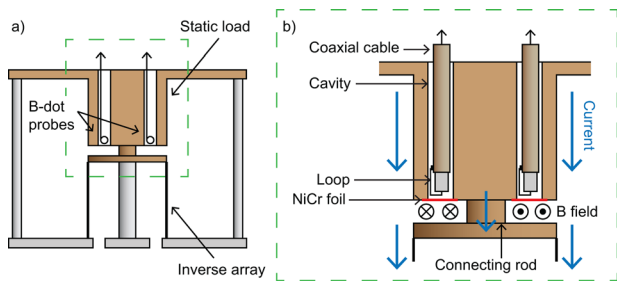
FIG. 7. Schematic of a B-dot diagnostic designed for monitoring *dI/dt* within a static load. B-dot probes formed from solid copper coaxial cable are inserted into cavities within a solid brass cylinder that acts as a static load array. Magnetic field surrounding the connecting rod penetrates the NiCr foil to generate voltage on the probes. The inverse array wires were removed for the calibration experiment.

through the section between the load and the inverse array fills the two cavities and is picked up by the embedded B-dots. The nominally identical probes were constructed by exposing and folding the inner conductor of a length of 0.02 in. semi-rigid coaxial cable back along a 0.5 mm long exposed length of dielectric and soldering to the cable outer conductor. The probes were insulated with Kapton® tube, and shielded with NiCr foil to mitigate against electrical noise whilst allowing penetration of magnetic flux into the cavities. The probes were positioned at the same radius but with opposite winding direction to allow discrimination between B-dot signals and possible capacitive coupling.

The sensitivity of the diagnostic depends on both the geometry of the probes and the extent to which magnetic flux is able to penetrate the cavity. Because of this, the diagnostic was calibrated experimentally using the same two-stage configuration, but with the inverse (exploding) array absent. In this case, all of the generator current flows through the load from the beginning of the current pulse. The known magnitude of the current (measured using our standard current diagnostics) was used to calibrate the probes.

The raw oscilloscope traces from the calibration experiment are shown in Fig. 8(a). The traces consist of opposite polarity *dB/dt* signals superimposed upon a common noise component. The opposite winding of the two probes allows the common signal (shown in blue) to be determined and subtracted from the data. The resulting *dB/dt* signal was calibrated against the known *dI/dt* of the generator from the same experiment. The result of this calibration is shown in Fig. 8(b). The good agreement in the temporal profiles of the generator *dI/dt* and the load *dI/dt* suggests that the probes function as expected and that their relative calibration is close.

C. Measurements of load *dI/dt* and the operation of a plasma flow-switch

The current diagnostic was fielded in place of the load (imploding) array, in a two-stage array configuration. The inverse (exploding) array was 16 mm Ø and consisted of 8, evenly distributed 12.5 μm Ø Al wires surrounding an 8 mm Ø cathode rod. A typical pair of oscilloscope B-dot signals measured during these experiments is shown in Fig. 9(a). It is seen that, accounting for their opposite polarity, the signals from the 2 probes agree reasonably well. The common noise
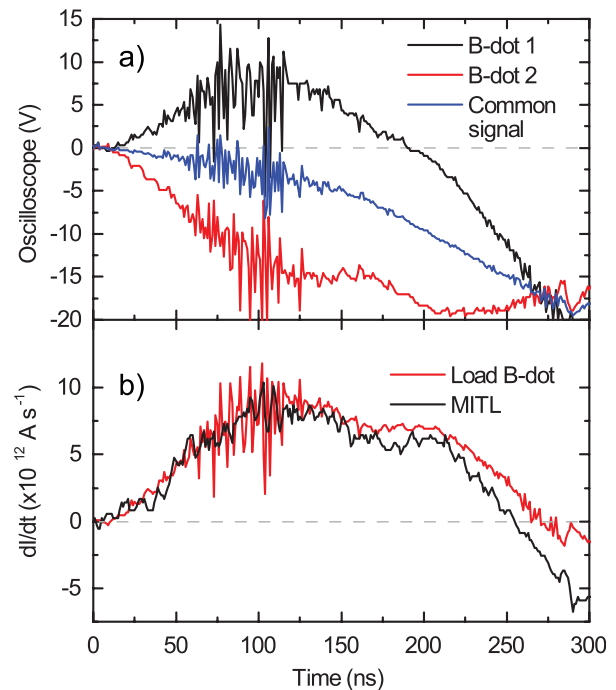

FIG. 8. Results from the B-dot calibration experiment. (a) Opposite polarity raw oscilloscope traces from the two B-dot probes and the deduced common signal component (blue line). (b) Calibration of the B-dot diagnostic against the MITL *dI/dt*.

component was subtracted, and the resulting signal scaled using the sensitivity from the calibration shot to give the pure *dI/dt* signal shown in Fig. 9(b). At the very beginning of the experiment, the *dI/dt* signal shows a short (∼15 ns) pre-pulse current in the load, which is driven by the increasing resistivity of the exploding array. The pre-pulse ends when the resistance of the inverse array collapses after formation of plasma on the wires. The duration of the pre-pulse is essentially the same as is observed in the case where a wire array is used instead of the static load. This supports the interpretation that during two-stage experiments with a wire array load, it is plasma formation on the exploder array wires that plays the key role in determining the duration of the pre-pulse, and not the increase of the resistance of the wires in the load array.

The switching of current into the static load starts at ∼125 ns. This is seen as a fast increase in the *dI/dt* in the load and from a decrease in the *dI/dt* of the generator current. The time of the switching is determined by the mass-per-unit-length and diameter of the exploding wire array, and is the same as observed in experiments using wire array loads instead of static loads. Note that the increase in *dI/dt* at the load exactly matches the time for the generator dip in *dI/dt*, suggesting the new diagnostic is sensitive to the beginning of the current switch, unlike the return post Rogowski measurements presented in Fig. 6. At ∼140 ns, the *dI/dt* signal in the load drops back through zero and begins to rise again only at ∼200 ns. This behaviour was unexpected and implies more complex evolution of the current switch.

To understand the behaviour of the signals, laser probing and XUV imaging of the load were performed at the time corresponding to the "pause" in the load *dI/dt*. The probing times are indicated by arrows in Fig. 9(b). The
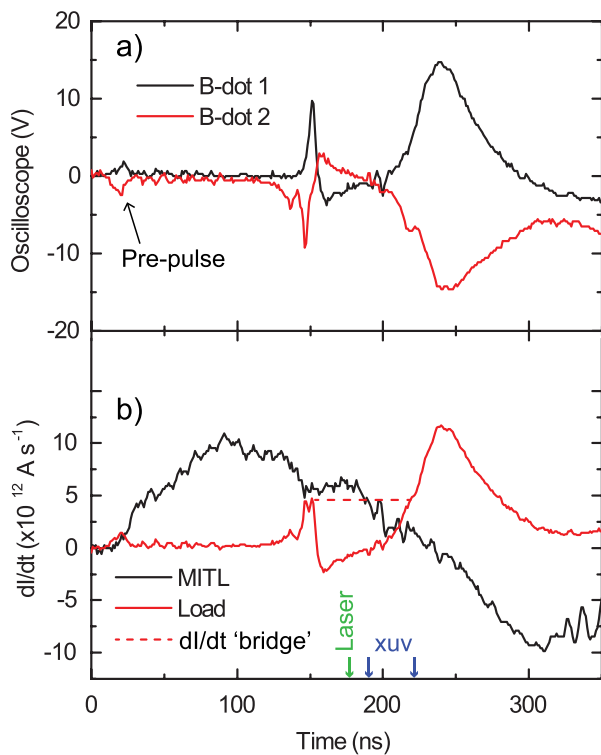
FIG. 9. Measurements of load *dI/dt* from the static B-dot diagnostic fielded in a two-stage array configuration. (a) Opposite polarity raw oscilloscope traces. (b) Load *dI/dt* (red line) deduced from signals in (a), together with generator *dI/dt* (black line) for comparison. Timings for laser probing and XUV images presented in Figs. 10(a) and 10(b) are indicated by arrows.

interferometry image in Fig. 10(a) and the first XUV self-emission frame in Fig. 10(b) show the presence of plasma in the load region, including in the gap between the load and the top electrode of the exploding array. The source of the plasma at the load appears to be an upward flow from the exploding inverse array beneath. The plasma in the gap provides an alternative current path to the rod connecting the exploding array to the load, and also shields the probes from magnetic flux. As a result, the B-dot probes are insensitive to changes in the load current until the implosion of the plasma in the region between the load and inverse arrays reopens the gap. The reopening of the gap can be seen in the second XUV frame shown in Fig. 10(b), obtained at 218 ns. Only after the probes "reopen" are they able to measure *dI/dt* in the load. Upward expansion of plasma from the inverse array towards the load has also been observed during experiments where the load was a wire array. The XUV self-emission frames in Fig. 10(c) clearly show the expansion of a plasma "bubble" as it bridges the section between the inverse and load arrays and initiates the current switch. XUV emission sequences in Figs. 11(a) and 11(b) show a radially outward expansion of plasma surrounding the load region. This is despite the $\mathbf{J} \times \mathbf{B}$ force acting radially inward on the load array, according to the array geometry presented in Fig. 1(a).

The combination of electrical measurements and imaging data suggests the following sequence of events during the current switch into the load, as illustrated in Fig. 12: As the outward motion of the inverse array begins, the increase in its resistance and inductance leads to a change in the partition of current between the inverse array and the load, and to the start of the main current switch. The initial load current rise is picked up by the embedded B-dot load. Some plasma from the inverse array then expands up toward the load array. The expanding magnetic cavity behaves as a plasma flow-switch and forms the current path shown in Fig. 12(b).
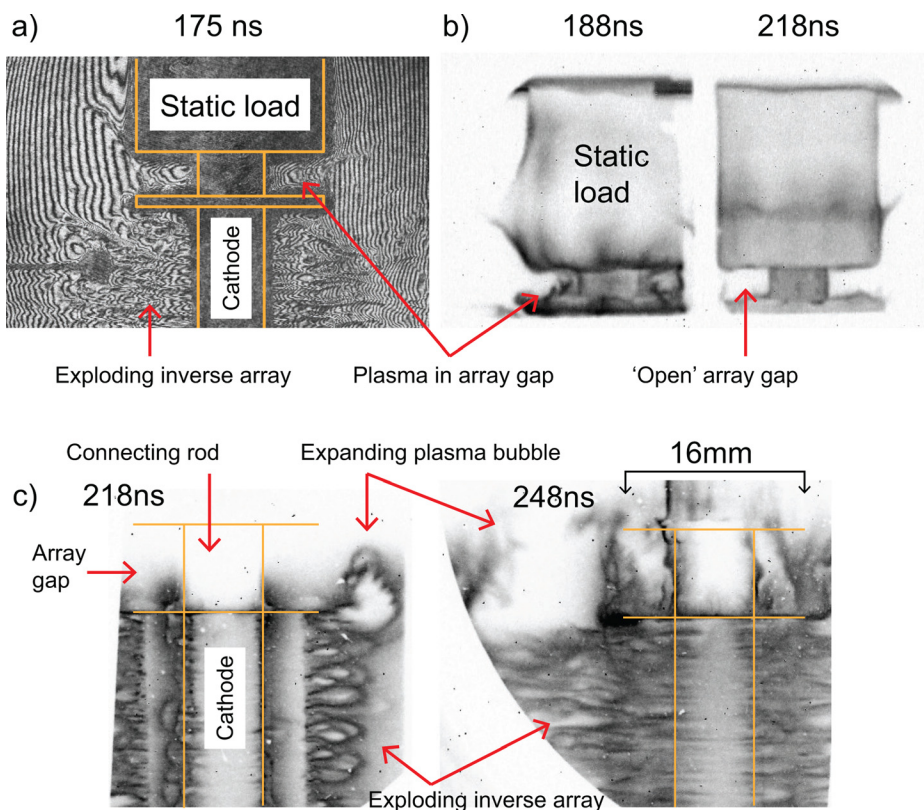

FIG. 10. Images showing plasma in the load region during the onset of the main current switch. Interferometry (a) and XUV emission images (b) from a static load experiment. The implosion of plasma in the array "gap" is clearly seen in the two XUV frames. (c) XUV sequence showing the expansion of a plasma "bubble" or magnetic cavity between the inverse and load arrays during a separate two-stage wire array experiment (same experiment as Fig. 2).
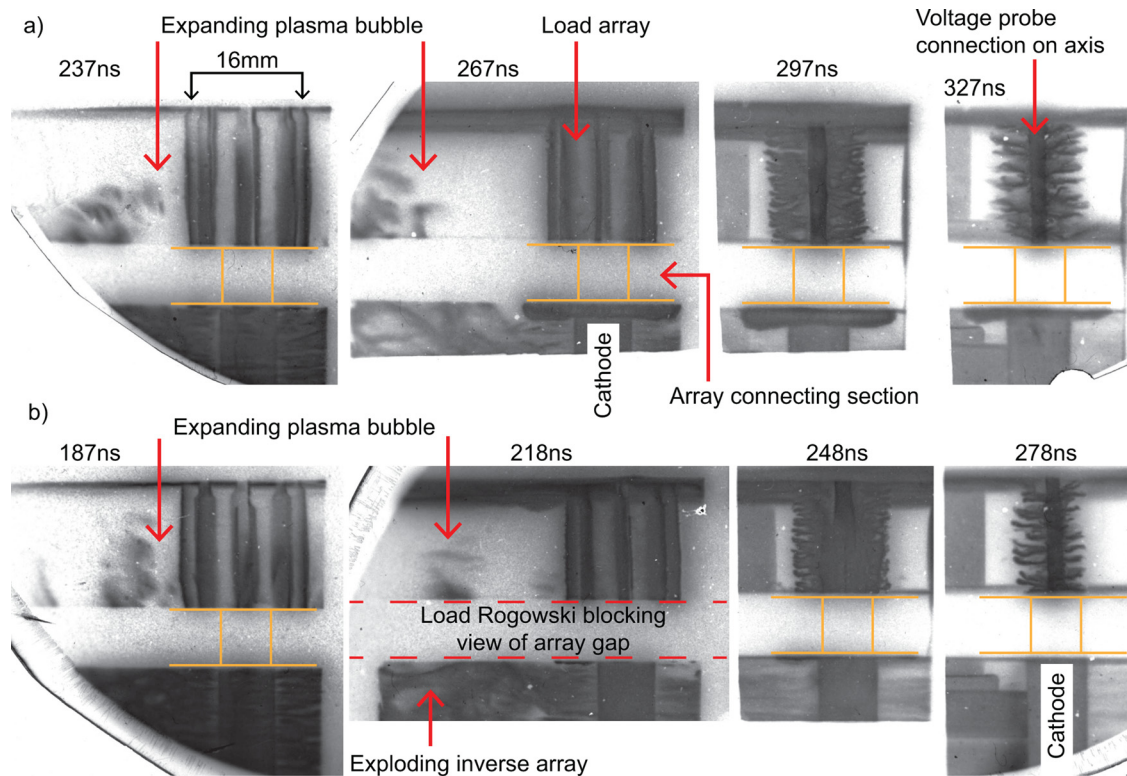
FIG. 11. XUV emission sequences from 27 mm and 24 mm load experiments (c.f. experiments in Sec. III) showing the expansion of a magnetic cavity around the load array and the subsequent load implosion. The axial voltage probe connection disrupts the stagnation of the pinch in these particular experiments. A load array Rogowski blocks the view of the inter-array section.

This plasma closes the gap between the load and the top electrode of the inverse array, preventing the B-dots within the stationary load of Fig. 7 from measuring the load current until it implodes and reopens the gap as illustrated in Fig. 12(c). Note that the current paths shown in Fig. 12 represent a simplified model for the real current paths, which are most likely radially distributed. The current flowing through the load is not required to return through the return posts, but could make partial use of the lower inductance path through the plasma of the exploding inverse array and the remnants of the expanded plasma bubble surrounding the load array. This could explain the delay and unusually small dI/dt signals observed with Rogowski probes installed on return posts, and the small $B(t)$ signals determined from Faraday rotation measurements taken high up in the current return structure. The existence of plasma and a possible return path surrounding the load probably explains why Rogowski

probes installed around the load array, as shown in Fig. 1(b), also do not function as initially expected.

Further evidence for the existence of the current path shown in Fig. 12 is observed as an axial zippering in the ionisation and emission from expanded wires upon switching. Data showing this are presented in Fig. 13. The XUV image in Fig. 13(a) shows emission localised at the cathode end of the load array. The two interferometry panels in Fig. 13(b) are taken from either end of a single interferogram. The inflection pattern of the interferometry fringes through the expanded wire cores changes significantly along the length of the load array, with direction and magnitude of the inflection indicating increased electron density toward the cathode. In addition, schliering of the interferometer probing beam due to radial electron density gradients at the wire edges creates shadowgraphy features in the lower interferogram and begins to deflect the probe out of the acceptance angle of the imaging system, causing a loss of the interference fringes. The zippering occurs on a timescale ($\sim$10 ns) much shorter than the timescale for the implosion of the array ($\sim$100 ns), and so does not have a detrimental effect on the implosion symmetry.

The onset of the current switch produces a significant decrease in the voltage on the MITL of the generator. This is because the rapidly changing geometry of the current path of the total load generates a large dL/dt. The MITL voltage can be used to estimate the change in the inductance of the load during the onset of the current switch. Without direct measurements of the load dI/dt due to reasons described in Sec. IV A, this analysis necessarily involves a comparison of
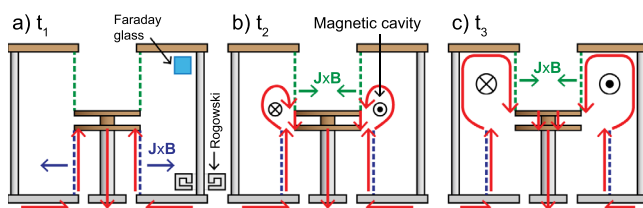

FIG. 12. Cartoon showing the evolution of a magnetic cavity acting as a plasma flow switch. The current paths (red lines) represent a simplification of the real, radially distributed current paths. Outward and upward motion of plasma from the inverse array initiates the current switch, which is further driven by rapid expansion of the annular plasma bubble. The B-dots in the static load are shielded during phase t_2.
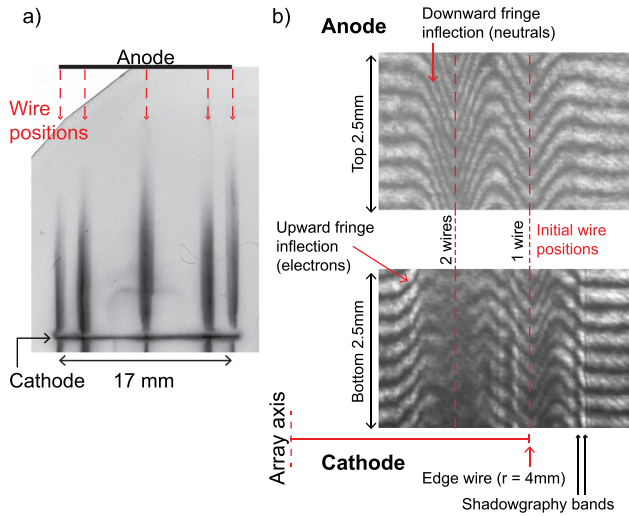
FIG. 13. Axially non-uniform plasma distribution during the onset of the current switch. (a) Enhanced XUV emission toward the cathode. (b) Cropped interferometry data from a single interferogram, showing three wires at either end of a 42 mm long load array. Two of these wires overlap along the line of sight. Greater electron density and sharper electron density gradients are observed toward the cathode. (a) and (b) Data are from two different experiments.

dI/dt signals from a two-stage wire array load with those from a static reference load. In addition, measurements of *dI/dt* are made using B-dot probes embedded in the MITL at a distance of roughly 30 cm from the load, and are only reliable so long as there is no electrical breakdown at the MITL neck. As a result, these calculations should be regarded as approximate but instructive.

The following formula describes the distribution of voltage over the system:

$$V_{G,0} = V_m + V_l. \tag{4}$$

In this equation, $V_{G,0}$ is the nominal driving voltage provided by the generator for a fixed inductance load. V_m is the voltage across the MITL, and V_l is the voltage across the load. V_m and V_l may, in general, apply to a static or dynamic ($\dot{L} \neq 0$) load. These voltages are given by the following expressions:

$$V_{G,0}(t) = L_0 \frac{dI_0(t)}{dt} = (L_m + L_{l,0}) \frac{dI_0(t)}{dt}, \tag{5a}$$

$$V_m(t) = L_m \frac{dI(t)}{dt}, \tag{5b}$$

$$V_l(t) = \frac{d}{dt}\left\{ L_l(t)I(t) \right\} + V_R(t)$$
$$= \frac{d}{dt}\left\{ (\delta L_l(t) + L_{l,0})I(t) \right\} + V_R(t). \tag{5c}$$

In these equations, I_0 is the current that flows through the fixed inductance load and I is the current that flows through the dynamic load. L_m is the fixed MITL inductance (12 nH), $L_{l,0}$ is the initial load inductance (10 nH), and $\delta L_l(t)$ is the change in the load inductance evaluated between t_0 and t. V_R is the resistive voltage drop across the load. The resistance of the MITL and fixed inductance load is assumed

negligible. Equations 5(a)–5(c) can be combined to give the following expression for the change in the inductance of the load:

$$\delta L(t) = \frac{1}{I(t)} \int_{t_0}^{t} (L_m + L_{l,0})\left\{ \frac{dI_0}{dt} - \frac{dI}{dt} \right\} - V_R(t) \ dt. \tag{6}$$

Analysis using Eq. (6) was performed for the same set of experiments described in Sec. III. The black line in Fig. 14 represents the nominal generator driving voltage waveform, dI_0/dt. This was determined via MITL B-dot measurements from a static load experiment with a load inductance similar to $L_{l,0}$. V_R was measured during two-stage array experiments using the method described in Sec. III. The blue line in Fig. 14 shows the full time scale for the voltage signal shown in Fig. 3. The probe measures 0 V between the pre-pulse and the current switch, indicating that it is not sensitive to magnetic flux during this time. The voltage probe provides meaningful data on load resistance so long as this is the case, and it has been assumed in the present analysis that the signal on the voltage probe remains purely resistive throughout the experiment. dI/dt for the two-stage array is shown as a red line. Significant deviation of V_m from $V_{G,0}$ occurs at a time corresponding to the beginning of emission from the load array as observed in optical streak images; this indicates a change in the load inductance as would be expected. The change in load inductance, δL_l, was calculated using Eq. (6) and is shown in green. The gentle increase in inductance from 110–185 ns could be due to radially outward advection of current within the inverse array ablation streams and also the expansion of the current path into the region between the load and inverse arrays. From 185–205 ns, there is a rapid increase in the load inductance that correlates well in time to the expansion of the plasma bubble observed with imaging diagnostics. After this time, the inductance continues to increase as current finds its new path through the load (imploding) array and the inverse array return path expands.

The inductance can be related to the effective geometry of the current carrying region to check the consistency of our plasma flow switch hypothesis. If we approximate the
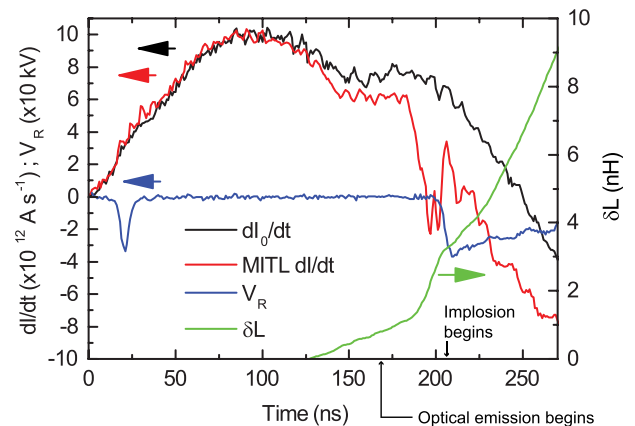

FIG. 14. *dI/dt* traces from a static load (black) and a two-stage wire array load (red). The signals deviate strongly during the main current switch. The resistive load voltage is shown in blue. These signals were used to determine the change in the load inductance (green) during current switch.

current path surrounding the expanding magnetic cavity as a cylindrically symmetric transmission line, then the additional inductance is given simply by

$$L = \frac{\mu_0 l}{2\pi} \ln \frac{R_o}{R_i}, \qquad (7)$$

where R_o and R_i are the radii of the outer and inner conductors, respectively, and l is the length of the transmission line. For a fixed inner radius (8 mm array radius), the inductance depends much more strongly on length than on outer radius. Therefore, for a poorly defined outer conductor radius, it is useful to make the approximation that $\dot{L} \propto dl/dt$. From Fig. 14, the inductance of the total load (inverse plus imploding array) changes by 2.4 nH between the beginning of the current switch (indicated by the onset of optical emission on the streak camera) and the start of the implosion. During this 30 ns interval, the average $\dot{L}$ is 0.08 nH/ns. Ignoring any effect from the exploding inverse array, this change in the load inductance corresponds to a change in the effective current path length of $\dot{l} = 1$ mm/ns, assuming $R_o = 12$ mm. This rate of transmission line expansion allows for the inclusion of the inductance of the full length of the load array (30 mm) before the beginning of the implosion. The effective current path geometry is consistent with XUV emission imaging data, as shown in Fig. 11.

Figure 10(c) shows the expansion of a plasma bubble just before the switch (the load array wires are not yet emitting XUV radiation), in the region between the inverse and load arrays. In this case, the geometry of the full plasma loop is better defined. R_i is at $r = 11$ mm, and the two time frames can be used to approximate Δl and ΔR_o as 6.5 mm. The expansion of this bubble suggests an $\dot{L}$ of $\sim$0.03 nH/ns, in agreement with the early time $\dot{L}$ given by the inductance trace in Fig. 14.

Further consistency with the flow switch mechanism is seen in the timing of the V_R signal. V_R begins to increase at 200 ns, implying an increase in the resistance of the inverse array long (40 ns) after the onset of the current switch into the load. Therefore, the switching mechanism cannot strongly depend on the inverse array resistance (although an increase in its inductance may still be important). The increased resistance could be caused by the highly non-uniform current return structure that forms when the inverse array explodes. The division of current between the load and inverse arrays is not known at this time in the experiment; therefore, the resistance of the inverse array upon switching cannot be accurately determined. Given the peak V_R of 37 kV, R ranges from 30–300 mΩ for current fractions of 100%–10% through the inverse array.

D. Estimates of load current

The shielding of the load B-dot probes by the plasma during the t_2 phase shown in Fig. 12 and their subsequent opening at a later time means that integration of the dI/dt signal as measured by the B-dots in Fig. 9 will produce a lower estimate for the magnitude of the current in the load. This estimate for the load current, together with the total generator current, is shown in Fig. 15 as the red line. It is seen that at least $\sim$700 kA switched into the load; however, it is unclear how to interpret the rise-time of this current pulse. The real current is

most probably considerably higher. The radial optical streak image in Fig. 16 shows the implosion of a typical wire array load in a two-stage array. The onset of optical emission corresponds to the beginning of the main current switch into the load array. Stagnation of the pinch according to the streak data occurs 95 ns later, at 230 ns. Previous work[23] has shown that as a result of wire conditioning by the small current pre-pulse (see Sec. III), all of the load array mass participates in the main implosion; there is very little or no pre-fill plasma within the array diameter, and no trailing mass. Consequently, a 0D implosion model[30] can be used to determine the current driving the implosion, given an implosion trajectory. The equation of motion for the imploding mass is given by

$$\hat{m}\ddot{r}(t) = -\frac{\mu_0 I(t)^2}{4\pi r(t)}, \qquad (8)$$

where $\hat{m}$ is the mass per unit length of the array and r is the array radius. The red line overlaid on the streak image in Fig. 16 represents a 0D implosion trajectory for the same $\hat{m}$ as the streak data, driven by the current measured by the B-dots on the static load (red line in Fig. 15). The 0D model converges on axis at 90 ns after the wire array load, indicating insufficient current is driving the model. An improved, but still conservative, estimate for the current can be obtained by assuming dI/dt remains constant during the period of B-dot shielding, at the value reached immediately before the onset of shielding. The "bridged" dI/dt trace for this situation looks like that shown as the dashed line in Fig. 9(b). The corresponding current trace and 0D implosion trajectories are plotted as blue lines in Figs. 15 and 16. In this scenario, the current reaches a peak of $\sim$1 MA in 150 ns. The 0D implosion trajectory once again indicates that this current profile is insufficiently steep to drive the observed implosion. However, the magnitude may be reasonable. Further 0D calculations suggest that for a linearly rising current drive, a 1.2 MA pulse with a 100 ns rise-time is required to match the implosion time of the load. This current pulse and the associated 0D implosion trajectory are plotted as green lines in Figs. 15 and 16. It is not possible to determine via the 0D implosion model the exact temporal current profile required to drive the experimentally observed rapid implosions. However, the calculations do
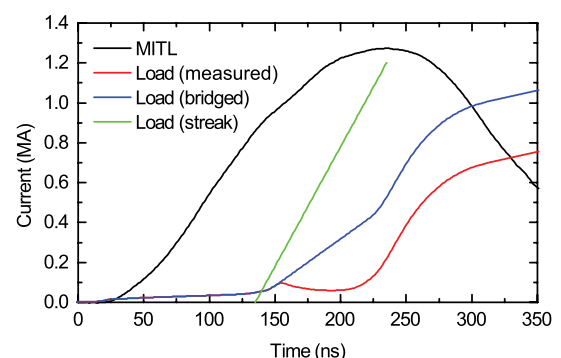

FIG. 15. Load current as seen by the static B-dot load (red) and the total generator (MITL) current from the same experiment (black). The blue current profile was calculated using the "bridged" dI/dt trace shown in Fig. 9. The green current profile generates a good fit of a 0D implosion model to optical streak data (see Fig. 16), but it is not a unique solution.
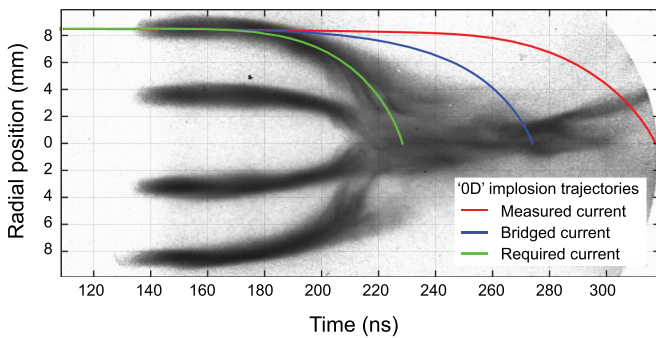
FIG. 16. Radial optical streak image showing the implosion of a 17 mm Ø, $8 \times 10 \,\mu m$ Al load array. The main current switch begins at 135 ns, giving an implosion time of ~95 ns. Implosion trajectories from a 0D implosion model are overlaid on the image. These trajectories were driven by the current pulses shown in Fig. 15.

indicate that the required average load dI/dt is approximately 1.2×10^{13} A s^{-1}, in excellent agreement with the peak value measured by the static load B-dots, as shown in Fig. 9(b). This value for dI/dt represents an approximate doubling of the average dI/dt of the generator. It should also be noted that no attempt has yet been made to optimise the system for the fastest current switch.

The current in the load remains to be accurately determined, although the new measurements are very useful in helping to construct the picture of the current switch mechanism. It may be possible to prevent the transient plasma shielding of the B-dot probes on Magpie experiments by using some dielectric shielding. However, it is not obvious that this could be achieved without disrupting the plasma flow switch mechanism. Nonetheless, it would be useful to determine the load current profile and observe the dynamics of the load array in the case where the plasma flow switch does not operate. To characterise the flow-switch more fully, Faraday rotation imaging will be performed during the switch on future experiments.

V. DISCUSSION ON THE SCALING OF THE TWO-STAGE Z-PINCH TO HIGHER CURRENT DEVICES

The interpretation of the current switching process is plausible but needs to be supported by additional measurements. Assuming the interpretation is correct, it has important implications for the operation of the two-stage array as a fast current switch and the scaling of the device to higher current machines. The formation of the plasma bubble propagating from the end of the exploding inverse array into the load region acts as a plasma flow switch, providing an additional current path that can rapidly shunt current into the load. As a result, switching into the load array does not entirely rely on the increase in impedance of the inverse array, as was previously thought. This result is important in the context of scaling to higher current machines: The resistive contribution to the impedance of the exploding inverse array likely scales undesirably with increased current because of the requirement for a larger initial array mass and the subsequent increase in conducting plasma density in the region surrounding the inverse array. In contrast, if the switching process relies more on the opening of the magnetically insulated cavity in Fig. 12, then

the performance of the switch may have a favourable scaling with generator current and could potentially be treatable with magneto-hydrodynamic (MHD) simulations. It is possible that even if the resistive impedance of the exploding array does not remain sufficiently high at large currents and associated high voltages, the flow-switch action could be sufficient for efficient operation of the switch.

The Magpie generator[24] used to perform the present experiments is a high impedance (1.25 Ω) machine. As a result, the drive current is very insensitive to the load inductance. The additional load inductance introduced by the extra length of a two-stage array would be an important consideration for a lower impedance machine such as the Z generator at Sandia National Laboratories because it will reduce the peak current delivered to the load. The initial inductance of the two-stage array can in fact be very low, as it is dominated by the inductance of the compact inverse array (red path in Fig. 1(a)). A realistic two-stage setup may consist of 1 cm long arrays, a central cathode rod diameter of 1.5 cm, array diameters of 2 cm, and a return structure diameter of (at most) 5 cm. For these numbers, and assuming coaxial symmetry (ignoring private wire inductance), the inductance of the inverse array is 0.6 nH.[25,31] The inductance will increase when current begins to switch into the load array. The upper limit for the inductance immediately after the main current switch (before the beginning of the implosion) will correspond to the blue path in Fig. 1(a) (i.e., will make full use of the return structure) and is equal to 4.2 nH for the numbers given above. The real inductance will likely be lower due to the radially distributed current path described earlier: For an effective return current path diameter of 3.5 cm, the corresponding inductance before the implosion is 2.8 nH. This inductance is comparable to the initial inductance of typical wire array loads on Z,[32] and so should not pose a problem in terms of maintaining the drive current at levels similar to those currently obtainable during the implosion phase of standard cylindrical wire arrays, when there is a large dL/dt. The two-stage array configuration introduces an additional dL/dt component during the current switching phase. In order to assess quantitatively the impact of this on the peak current delivered to the load array, it will be necessary to model the plasma bubble motion from the inverse wire array. Such modeling should be possible with existing MHD codes, but this is beyond the scope of this paper.

The most powerful x-ray sources fielded on Z already include a type of inductive switch in the form of a concentric large diameter wire array.[1,31,33] It is interesting to compare this "nested" configuration with the operation of the two-stage array described in the present paper. In a nested load configuration, the outer array inductively shields an inner array from the generator current during the ablation phase and the beginning of the snowplough implosion. When the imploding current sheath reaches the radius of the inner array, some fraction of the current switches from the outer to the inner. This drives a second ablation phase, snowplough implosion and stagnation of the inner array onto the axis. The rapid current shunt and the resulting fast implosion from an initially small radius may explain the high x-ray power output of nested implosions. To an extent, the action of this switch is to reset the initial

conditions for the implosion at a smaller radius. There is effectively a large radial convergence of the current sheath (from the initial outer to initial inner radius) with much reduced associated growth of the MRT instability amplitude.

Despite the favourable performance of a nested array over the equivalent standard array, there remain some issues that limit their efficiency. First, although improved, the final implosion remains non-uniform. Instabilities in the outer array imprint to some extent on the inner array during switching, and the inner array undergoes an axially modulated ablation phase before imploding. Second, the mass of the outer array ends up being included in the final implosion, limiting the implosion velocity. Third, the trailing mass from both the inner and outer array implosions provides a large radius, low inductance current path that limits the current convergence and the plasma compression at stagnation.

Many wire array z-pinch configurations have been shown to exhibit similar behavior when driven by peak currents ranging from 1–20 MA. The two-stage array presented here could potentially provide a means for rapid switching at the 20 MA level into a wire array with a diameter comparable to that of a typical nested inner array, with the benefit of very uniform initial conditions for the final implosion enabled by the pre-pulse and dwell phase. Previous work[23] has shown that perturbations to the preconditioned wire core surfaces are not more than $1.5 \, \mu m$ in size. In addition, negligible mass (not more than a few % from imaging diagnostics) from the inverse (switch) array is included in the final implosion, allowing for faster implosion velocities and minimal imprint from the inverse array history onto the load array. The proximity of the inverse array to the load, together with the axial evolution of the flow switch, does impose an ionisation zippering on the load array. However, this occurs on a timescale much less than the implosion time for the array, and time-gated XUV emission and laser probing images show that the load array implodes uniformly along its length. The uniformity of the preconditioned wires and the bulk ionisation upon current switching results in very little or no trailing mass at large radius during the final implosion.

The initial conditions for the final implosion and the large dI/dt into the load array may favour a higher power x-ray source than a standard cylindrical array or a nested array. However, we stress that at this time we have not performed systematic studies of the x-ray output or attempted to optimise the array geometry for this means, concentrating instead on an understanding of the preconditioning and the mechanism for the main current switch. Therefore, at the present time we do not have the information to make quantitative comparisons between nested arrays and two-stage arrays in terms of their x-ray output. During standard wire array implosions the ablation phase radially redistributes the array mass prior to the main implosion. The prefill plasma helps to reduce the growth of the MRT instability by reducing the acceleration of the bulk array mass during the snowplough-like implosion phase. In the present setup the absence of a load array ablation phase leads to a 0D-like, accelerating final implosion, which consequently becomes MRT unstable despite the uniform initial conditions. However, the system may allow for carefully tailored radial mass distributions such as preconditioned, nested plasma shells that could be optimised for implosion stability and heating at stagnation. With the means to generate 0D-like implosions, it is now also possible to study more exotic potential MRT mitigation techniques, such as introducing axial or cusp magnetic fields.[30]

VI. CONCLUSIONS

We have described the operation of a two-stage wire array z-pinch driven by the 1.4 MA, 240 ns Magpie pulsed-power device. This setup is used to both precondition a cylindrical load array and significantly sharpen the dI/dt provided by the generator in a very economical way. In the two-stage configuration, an inverse wire array acts as a fast current switch, delivering a current pre-pulse into the cylindrical load array, before rapidly switching the majority of the generator current into the load after a $\sim$100 ns dwell time. The pre-pulse and dwell time result in uniform expansion of the load array wire cores prior to the implosion, dramatically altering the implosion dynamics of the load array upon the main current switch. Analysis of imaging and electrical data suggests that the main current switch evolves in part as a plasma flow switch, driven by the expansion of a magnetic cavity and plasma bubble along the length of the load array. Load implosion times indicate that the flow switch sharpens the generator dI/dt by a factor of $\sim$2. It would be very interesting to field the two-stage wire array z-pinch load on a higher current, lower impedance facility. This type of flow switch may scale favourably to larger generators because the magnetic cavity will be driven faster by a larger current. The operation of the switch does not depend entirely on increased impedance of the inverse array, a detail which could otherwise be problematic on machines operating at higher voltage and with greater plasma densities. A drop in the peak load current must result when sharpening dI/dt in this way. However, the extra load inductance introduced by the inverse array is a relatively small addition to the total load inductance, so this effect may be manageable. MHD simulations of the plasma bubble motion are required before a meaningful circuit analysis can be performed. This load configuration could potentially be applied as a high power x-ray source. Previous work has shown[4,34] that x-ray yields from wire array implosions have a favourable scaling with dI/dt, which may be significantly increased in the present setup. In addition, the preconditioning of the load array results in very uniform initial conditions for the final implosion, negligible trailing mass, and the possibility to carefully tailor the radial mass distribution to optimise implosion stability and stagnation heating.

[1]M. E. Cuneo, D. B. Sinars, E. M. Waisman, D. E. Bliss, W. A. Stygar, R. A. Vesey, R. W. Lemke, I. C. Smith, P. K. Rambo, J. L. Porter, G. A. Chandler, T. J. Nash, M. G. Mazarakis, R. G. Adams, E. P. Yu, K. W. Struve, T. A. Mehlhorn, S. V. Lebedev, J. P. Chittenden, and C. A. Jennings, Phys. Plasmas **13**(5), 056318 (2006).

[2]D. J. Ampleford, B. Jones, C. A. Jennings, S. B. Hansen, M. E. Cuneo, A. J. Harvey-Thompson, G. A. Rochau, C. A. Coverdale, A. R. Laspe, T. M. Flanagan, N. W. Moore, D. B. Sinars, D. C. Lamppa, E. C. Harding, J. W. Thornhill, J. L. Giuliani, Y.-K. Chong, J. P. Apruzese, A. L. Velikovich, A. Dasgupta, N. Ouart, W. A. Sygar, M. E. Savage, J. K. Moore, R. Focia, T. C. Wagoner, K. L. Killebrew, A. D. Edens, G. S. Dunham, M. C. Jones, P. W. Lake, D. S. Nielsen, M. Wu, A. L. Carlson, M. D. Kernahan, C. R. Ball, R. D. Scharberg, T. D. Mulville, E. W. Breden, C. S. Speas, G. Olivas, M. A. Sullivan, A. J. York, D. W. Justus, J. C. Cisneros, T. Strizic, J. Reneker, M. Cleveland, M. P. Vigil, G. Robertson, D. Sandoval, C. Cox, A. J. Maurer, D. A. Graham, N. B. Huynh, S. Toledo, L. P. Molina, M. R. Lopez, F. W. Long, G. R. McKee, J. L. Porter, and M. C. Herrmann, Phys. Plasmas **21**(5), 056708 (2014).

[3]M. E. Cuneo, R. A. Vesey, D. B. Sinars, J. P. Chittenden, E. M. Waisman, R. W. Lemke, S. V. Lebedev, D. E. Bliss, W. A. Stygar, J. L. Porter, D. G. Schroen, M. G. Mazarakis, G. A. Chandler, and T. A. Mehlhorn, Phys. Rev. Lett. **95**, 185001 (2005).

[4]W. A. Stygar, M. E. Cuneo, R. A. Vesey, H. C. Ives, M. G. Mazarakis, G. A. Chandler, D. L. Fehl, R. J. Leeper, M. K. Matzen, D. H. McDaniel, J. S. McGurn, J. L. McKenney, D. J. Muron, C. L. Olson, J. L. Porter, J. J. Ramirez, J. F. Seamen, C. S. Speas, R. B. Spielman, K. W. Struve, J. A. Torres, E. M. Waisman, T. C. Wagoner, and T. L. Gilliland, Phys. Rev. E **72**, 026404 (2005).

[5]S. A. Chaikovsky, V. A. Kokshenev, A. G. Rousskikh, A. V. Shishlov, A. V. Fedunin, A. Yu. Labetsky, N. E. Kurmaev, and F. I. Fursov, AIP Conf. Proc. **808**(1), 41 (2006).

[6]A. Kingsep, Yu. Bakshaev, A. Bartov, P. Blinov, A. Chernenko, R. Chikin, K. Chukbar, S. Danko, L. Dubas, Yu. Kalinin, I. Kovalenko, A. Lobanov, V. Mizhiritsky, V. Shchagin, and V. Smirnov, in *Proceedings of 14th IEEE International Pulsed Power Conference* (2003), Vol. 1, p. 689.

[7]F. S. Felber, E. M. Waisman, and M. G. Mazarakis, Phys. Rev. Lett. **104**, 185001 (2010).

[8]P. J. Turchi, M. L. Alme, G. Bird, C. N. Boyer, S. K. Coffey, D. Conte, J. F. Davis, and S. W. Seiler, IEEE Trans. Plasma Sci. **15**(6), 747 (1987).

[9]P. F. Ottinger, S. A. Goldstein, and R. A. Meger, J. Appl. Phys. **56**(3), 774 (1984).

[10]B. V. Weber, R. J. Commisso, P. J. Goodrich, J. M. Grossmann, D. D. Hinshelwood, J. C. Kellogg, and P. F. Ottinger, IEEE Trans. Plasma Sci. **19**(5), 757 (1991).

[11]C. W. Mendel and S. A. Goldstein, J. Appl. Phys. **48**(3), 1004 (1977).

[12]B. V. Weber, R. J. Commisso, G. Cooperstein, J. M. Grossmann, D. D. Hinshelwood, D. Mosher, J. M. Neri, P. F. Ottinger, and S. J. Stephanakis, IEEE Trans. Plasma Sci. **15**(6), 635 (1987).

[13]J. R. Thompson, P. L. Coleman, R. J. Crumley, P. J. Goodrich, J. R. Goyer, J. E. Rauch, J. J. Moschella, and E. J. Yadlowsky, in *Proceedings of the 12th International Conference on High-Power Particle Beams* (1998), Vol. 1, p. 338.

[14]P. Coleman, J. Rauch, W. Rix, J. Thompson, and R. Wilson, AIP Conf. Proc. **409**, 119 (1997).

[15]J. Thompson, P. Coleman, D. Parks, E. Waisman, W. Rix, M. Babineau, V. Kenyon, G. L. Whitehead, P. Corcoran, R. Crumley, M. Danforth, J. Douglas, P. Spence, P. Steen, T. Tucker, P. Kurucz, and K. Ware, in *Proceedings of IEEE Pulsed Power Plasma Science Conference* (2001), Vol. 1, p. 657.

[16]S. V. Lebedev, F. N. Beg, S. N. Bland, J. P. Chittenden, A. E. Dangor, M. G. Haines, K. H. Kwek, S. A. Pikuz, and T. A. Shelkovenko, Phys. Plasmas **8**, 3734 (2001).

[17]V. V. Alexandrov, I. N. Frolov, M. V. Fedulov, E. V. Grabovsky, K. N. Mitrofanov, S. L. Nedoseev, G. M. Oleinik, I. Yu. Porofeev, A. A. Samokhin, P. V. Sasorov, V. P. Smirnov, G. S. Volkov, M. M. Zurin, and G. G. Zukakischvili, IEEE Trans. Plasma Sci. **30**(2), 559 (2002).

[18]M. E. Cuneo, E. M. Waisman, S. V. Lebedev, J. P. Chittenden, W. A. Stygar, G. A. Chandler, R. A. Vesey, E. P. Yu, T. J. Nash, D. E. Bliss, G. S. Sarkisov, T. C. Wagoner, G. R. Bennett, D. B. Sinars, J. L. Porter, W. W. Simpson, L. E. Ruggles, D. F. Wenger, C. J. Garasi, B. V. Oliver, R A. Aragon, W. E. Fowler, M. C. Hettrick, G. C. Idzorek, D. Johnson, K. Keller, S. E. Lazier, J. S. McGurn, T. A. Mehlhorn, T. Moore, D. S. Nielsen, J. Pyle, S. Speas, K. W. Struve, and J. A. Torres, Phys. Rev. E **71**, 046406 (2005).

[19]I. Blesener, B. Kusse, K. Blesener, J. Greenly, and D. Hammer, IEEE Trans. Plasma Sci. **40**(12), 3313 (2012).

[20]G. F. Swadling, S. V. Lebedev, N. Niasse, J. P. Chittenden, G. N. Hall, F. Suzuki-Vidal, G. Burdiak, A. J. Harvey-Thompson, S. N. Bland, P. De Grouchy, E. Khoory, L. Pickworth, J. Skidmore, and L. Suttle, Phys. Plasmas **20**(2), 022705 (2013).

[21]G. F. Swadling, S. V. Lebedev, G. N. Hall, F. Suzuki-Vidal, G. Burdiak, A. J. Harvey-Thompson, S. N. Bland, P. De Grouchy, E. Khoory, L. Pickworth, J. Skidmore, and L. Suttle, Phys. Plasmas **20**(6), 062706 (2013).

[22]S. V. Lebedev, F. N. Beg, S. N. Bland, J. P. Chittenden, A. E. Dangor, and M. G. Haines, Phys. Plasmas **9**(5), 2293 (2002).

[23]A. J. Harvey-Thompson, S. V. Lebedev, G. Burdiak, E. M. Waisman, G. N. Hall, F. Suzuki-Vidal, S. N. Bland, J. P. Chittenden, P. De Grouchy, E. Khoory, L. Pickworth, J. Skidmore, and G. Swadling, Phys. Rev. Lett. **106**, 205002 (2011).

[24]I. H. Mitchell, J. M. Bayley, J. P. Chittenden, J. F. Worley, A. E. Dangor, M. G. Haines, and P. Choi, Rev. Sci. Instrum. **67**(4), 1533 (1996).

[25]A. J. Harvey-Thompson, S. V. Lebedev, S. N. Bland, J. P. Chittenden, G. N. Hall, A. Marocchino, F. Suzuki-Vidal, S. C. Bott, J. B. A. Palmer, and C. Ning, Phys. Plasmas **16**(2), 022701 (2009).

[26]G. N. Hall, S. V. Lebedev, F. Suzuki-Vidal, G. Swadling, J. P. Chittenden, S. N. Bland, A. Harvey-Thompson, P. F. Knapp, I. C. Blesener, R. D. McBride, D. A. Chalenski, K. S. Blesener, J. B. Greenly, S. A. Pikuz, T. A. Shelkovenko, D. A. Hammer, and B. R. Kusse, Phys. Plasmas **20**(2), 022703 (2013).

[27]G. C. Burdiak, S. V. Lebedev, G. N. Hall, A. J. Harvey-Thompson, F. Suzuki-Vidal, G. F. Swadling, E. Khoory, L. Pickworth, S. N. Bland, P. de Grouchy, and J. Skidmore, Phys. Plasmas **20**(3), 032705 (2013).

[28]V. V. Aleksandrov, A. G. Alekseev, V. N. Amosov, M. M. Basko, G. S. Volkov, E. V. Grabovskii, A. V. Krasil'nikov, G. M. Oleinik, I. N. Rastyagaev, P. V. Sasorov, A. A. Samokhin, V. P. Smirnov, and I. N. Frolov, Plasma Phys. Rep. **29**, 1034 (2003).

[29]G. F. Swadling, "An experimental investigation of the azimuthal structures formed during the ablation phase of wire array z-pinches," Ph.D. thesis, Imperial College London, 2012.

[30]D. D. Ryutov, M. S. Derzon, and M. K. Matzen, Rev. Mod. Phys. **72**, 167 (2000).

[31]A. L. Velikovich, I. V. Sokolov, and A. A. Esaulov, Phys. Plasmas **9**(4), 1366 (2002).

[32]E. M. Waisman, M. E. Cuneo, W. A. Stygar, R. W. Lemke, K. W. Struve, and T. C. Wagoner, Phys. Plasmas **11**(5), 2009 (2004).

[33]J. Davis, N. A. Gondarenko, and A. L. Velikovich, Appl. Phys. Lett. **70**, 170 (1997).

[34]D. B. Sinars, R. W. Lemke, M. E. Cuneo, S. V. Lebedev, E. M. Waisman, W. A. Stygar, B. Jones, M. C. Jones, E. P. Yu, J. L. Porter, and D. F. Wenger, Phys. Rev. Lett. **100**, 145002 (2008).